Improving the Morphology Stability of Spiro-OMeTAD Films for
Enhanced Thermal Stability of Perovskite Solar Cells
Peer-reviewed author version

SONG, Wenya; Rakocevic, Lucija; THIRUVALLUR EACHAMBADI, Ragha; Qiu,
Weiming; Bastos, Joao P.; Gehlhaar, Robert; KUANG, Yinghuan; Hadipour, Afshin;
AERNOUTS, Tom & POORTMANS, Jef (2021) Improving the Morphology Stability of
Spiro-OMeTAD Films for Enhanced Thermal Stability of Perovskite Solar Cells. In:
Acs Applied Materials & Interfaces, 13 (37) , p. 44294 -44301.

Improving the Morphology Stability of Spiro-OMeTAD Films for Enhanced Thermal Stability of Perovskite Solar Cells

Wenya Song[1,2]*, Lucija Rakocevic[1,2], Raghavendran Thiruvallur Eachambadi[3], Weiming Qiu[2,4], João P. Bastos[4], Robert Gehlhaar[4], Yinghuan Kuang[1], Afshin Hadipour[1], Tom Aernouts[1], Jef Poortmans[1,2,5]*

1. imec - Partner in Solliance and Energyville, Thor Park 8320, 3600 Genk, Belgium

2. Katholieke Universiteit Leuven, Department of Electrical Engineering (ESAT), Kasteelpark Arenberg 10, 3001 Heverlee, Belgium

3. UHasselt - X-LAB, Agoralaan, 3590 Diepenbeek, Belgium

4. imec, Kapeldreef 75, 3001 Leuven, Belgium

5. UHasselt, Institute for Materials Research (IMO-IMOMEC), Agoralaan, 3590 Diepenbeek, Belgium

ABSTRACT

To guarantee a long lifetime of perovskite-based photovoltaics, the selected materials need to survive relatively high temperature stress during the solar cell operation. Highly efficient n-i-p perovskite solar cells (PSCs) often degrade at high operational temperatures due to morphological instability of the hole transport material 2,2',7,7'-tetrakis (N, N-di-p-methoxyphenyl-amine)9,9'-spirobifluorene (Spiro-OMeTAD). We discovered that the detrimental large domain spiro-OMeTAD crystallization is caused by the simultaneous presence of tert-butylpyridine (tBP) additive and gold (Au) as capping layer. Based on this discovery and our understanding, we demonstrated facile strategies that successfully stabilize the amorphous phase of spiro-OMeTAD film. As a result, the thermal stability of n-i-p PSCs is largely improved. After the spiro-OMeTAD films in the PSCs were stressed for 1032 hours at 85 °C in darkness in nitrogen environment, reference PSCs retained only 22% of their initial average power conversion efficiency (PCE), while the best target PSCs retained 85% relative average PCE. Our work suggests facile ways to realize efficient and thermally stable spiro-OMeTAD containing n-i-p PSCs.

TOC GRAPHICS
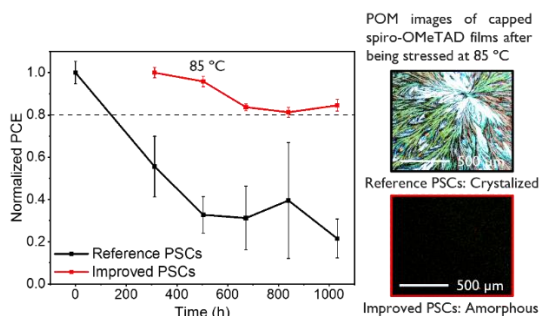
1. INTRODUCTION

Thin film solar cells based on halide perovskite have reached efficiencies above 25%[1], quickly catching up with the most advanced silicon-based solar cell efficiencies. This makes perovskite photovoltaics (PV) a potentially strong player in future PV markets. Certainly, one of the preconditions for commercialization of a PV technology is its performance stability. During the lifetime of PV panels, they are expected to perform well despite various stresses, including temperature, illumination, and atmospheric components, such as oxygen and moisture. While the effect of atmospheric components can be significantly mitigated by encapsulation[2–4], temperature and illumination are intrinsically imposed on solar cells. When a perovskite solar cell (PSC) is exposed to high atmospheric temperature and strong irradiance, its temperature can easily reach 60 °C[5]. Not to mention, the temperature of an insulated building-integrated PV panel can exceed 90 °C[6]. Thus, it is necessary to develop stable solar cell stacks that can withstand this high temperature.

Nowadays, the most efficient PSCs are realized using n-i-p configuration with amorphous 2,2',7,7'-tetrakis(N,N-di-p-methoxyphenyl-amine)9,9'-spirobifluorene (spiro-OMeTAD) as hole transport layer in combination with gold (Au) contact, which delivers outstanding power conversion efficiency (PCE) over 23%[7–10]. However, these PSCs are not stable at high temperatures due to the morphology instability of spiro-OMeTAD films[11–13]. Usually, spiro-OMeTAD solution is coated onto perovskite layer and fast dried, resulting in a smooth amorphous film. Other than spiro-OMeTAD molecules themselves, the presence of additional molecules is required to enhance the hole transporting capability and conductivity of the film. The prevalent practice is to use the combination of lithium bis(trifluoromethanesulfonyl)imide (Li-TFSI) and tert-butylpyridine (tBP). Li-TFSI oxidizes spiro-OMeTAD into Spiro-OMeTAD[+], which acts as

the acceptor, facilitating hole transport[14], thus increasing electrical mobility and conductivity of the spiro-OMeTAD film[15,16]. tBP molecules are used to increase the solubility of Li-TFSI in spiro-OMeTAD molecules matrix[17]. Malinauskas et al.[12] pointed out the low glass transition temperature (Tg) molecules tBP act as plasticizers in the amorphous spiro-OMeTAD films. As a result, the spiro-OMeTAD films crystalize at lower temperature, decreasing their morphological stability. On the other hand, depositing a metal like silver (Ag) on top of amorphous spiro-OMeTAD also facilitates its crystallization[12], yet the mechanism behind this phenomena is still not fully understood. Increasing the Tg of spiro-OMeTAD films is an obvious way to prevent the spiro-OMeTAD crystallization. Malinauskas et al.[12] tried to increase the Tg of the films by using modified spiro-OMeTAD molecules, i.e. using spiro-OMeTAD molecules with ligands. Zhang et al.[18] also improved the morphology stability of spiro-OMeTAD films by replacing Li-TFSI and tBP additives with TBATFSI or TBAPF$_6$ to get rid of the low Tg tBP molecules. Ren et al.[19] mixed high Tg polymer poly(9-vinylcarbazole) (PVK) with oxidized spiro-OMeTAD, increasing the Tg of spiro-OMeTAD film by 28 °C thus stabilizing its morphology. Apart from increasing the Tg of the spiro-OMeTAD films, some researchers attempted to directly deposit crystalline spiro-OMeTAD so that the PSCs do not suffer from the phase transition of spiro-OMeTAD films. Barranco[20] et al. sublimated dopant-free crystalline spiro-OMeTAD onto perovskite, leading to better PSC thermal stability. However, the PSCs containing sublimated crystalline spiro-OMeTAD were not yet able to reach high PCEs as those containing solution processed spiro-OMeTAD. Despite all these precedent work, facile ways to improve the morphology stability of spiro-OMeTAD films are still desired. Here in this work, we first analyzed the causes for the unfavorable large domain spiro-OMeTAD crystallization. We discovered the spiro-OMeTAD crystallization is caused by the simultaneous presence of tBP and Au capping layer. According to this discovery

and our understanding, facile methods were demonstrated to successfully stabilize the amorphous phase of spiro-OMeTAD, leading to largely improved PSC thermal stability.

2. RESULTS AND DISCUSSION

2.1. Causes for spiro-OMeTAD film crystallization.

Our analysis involved 48 n-i-p PSCs with the structure of glass/150 nm indium tin oxide (ITO)/20 nm SnO_2/3 nm phenyl-C61-butyric acid methyl ester (PCBM)/450 nm perovskite/250 nm spiro-OMeTAD/80 nm Au. With 24 PSCs the spiro-OMeTAD films contain both Li-TFSI and tBP, while those in the rest 24 PSCs contain only Li-TFSI. These PSCs were stressed at test standard temperature of 85 °C[21] in darkness in nitrogen environment for 1032 hours. Current density-voltage (JV) measurements were performed every 6 to 8 days to track their performance. As can be seen from Figure 1 (a), though the PSCs with only Li-TFSI have relatively low initial efficiency of about 10%, they are stable through the 1032 hours of thermal stressing. In contrast, the PSCs with both Li-TFSI and tBP show drastic decrease in average efficiency from 15% to lower than 3% already within the first 200 hours of thermal stressing. The decrease in efficiency is mainly attributed to the decrease in short circuit current density (Jsc) and fill factor (FF), as shown in Figure S1 and the red JV curve in Figure 2. After the thermal stressing, part of the Au electrode is removed and the morphology of the underlying spiro-OMeTAD film was examined using polarized optical microscope (POM) and scanning electron microscope (SEM). The POM images in Figure 1 (b and c) show that the spiro-OMeTAD film with solely Li-TFSI remained amorphous, while the one with both Li-TFSI and tBP crystallized at the area capped by Au. The top-view and cross-section view SEM images in Figure 1 (b1 and b2) reveal that although some aggregates[22] and holes[11] were present on top and in the spiro-OMeTAD film with only Li-TFSI, the film remained continuous. In contrast, empty trenches of several micrometers were

created in the crystallized spiro-OMeTAD film as shown in Figure 1 (c1 and c2). From these results, it can be readily concluded that the presence of tBP is essential for the occurrence of large domain spiro-OMeTAD film crystallization. Interestingly, Figure 1 (c, c3 and c4) reveal that the uncapped spiro-OMeTAD mostly stays amorphous and smooth. Only a few small crystals are present in this area, which are labeled by yellow circles in Figure 1 (c). The SEM images in Figure S2 reveal that these small crystals are up to about 10 µm large. They ceased growing because a gap was generated between the amorphous and crystalline spiro-OMeTAD. Hence, by comparing the Au-capped spiro-OMeTAD and the uncapped Spiro-OMeTAD in Figure 1 (c, c1-c4), it can be deduced that Au-capped spiro-OMeTAD and uncapped spiro-OMeTAD can both crystalize, however, the presence of Au capping layer is essential for the occurrence of large domain spiro-OMeTAD crystallization. Therefore, it can be concluded that the large domain spiro-OMeTAD crystallization and the resultant emergence of micrometer size trenches require the presence of both tBP and Au capping layer.
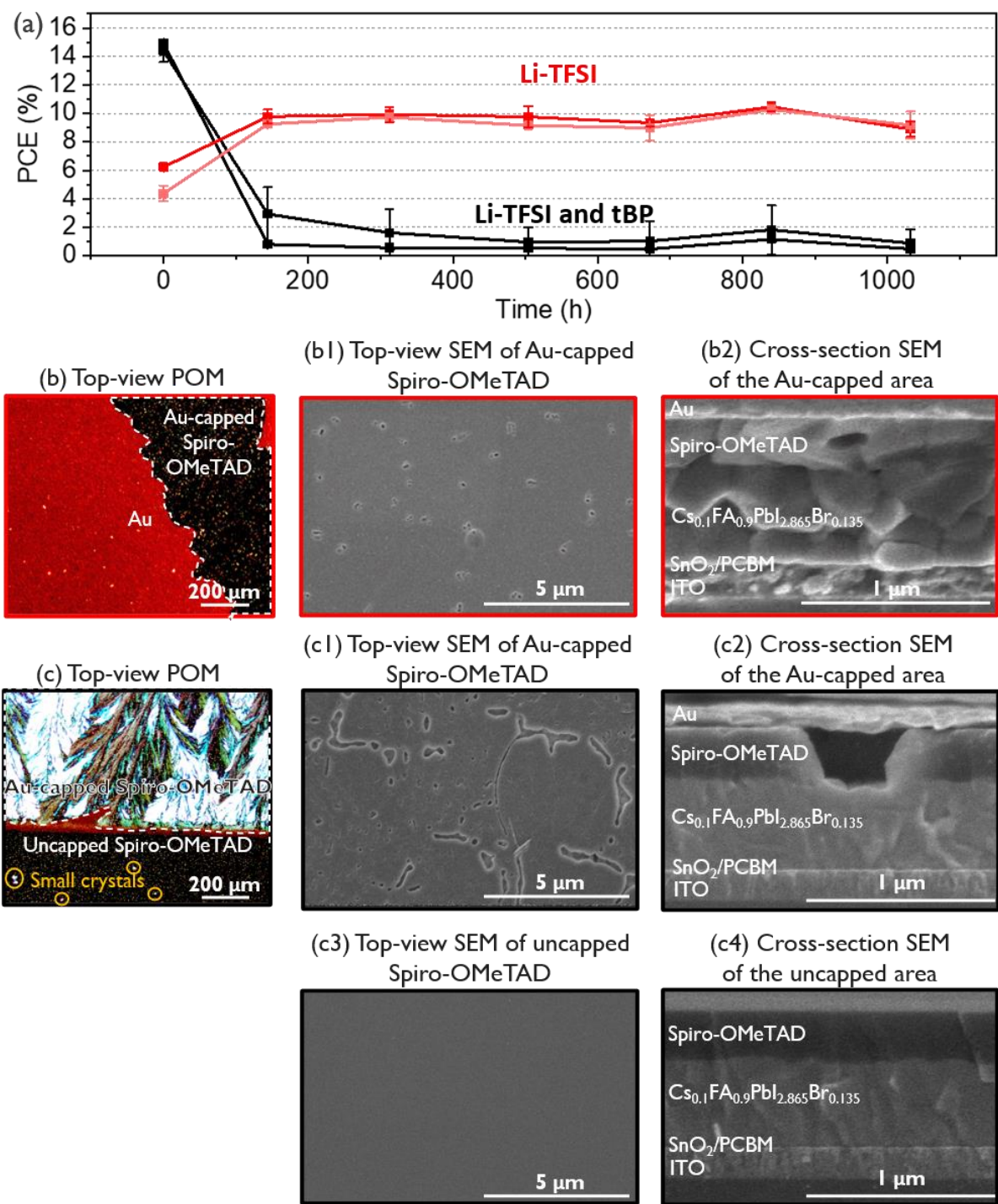
Figure 1. (a) Power conversion efficiency (PCE) evolvement of PSCs under 85 °C thermal stress. Each data point represents mean value of 12 PSCs on one substrate and the error bars indicate the standard deviation. (b, b1, b2) Top-view POM image, top-view SEM image and cross-section SEM

image of the stressed PSCs with only Li-TFSI additive. In (b), the area encircled by white dashed line was originally capped by Au. (c, c1, c2) Top-view POM image, top-view SEM image and cross-section SEM image of the stressed PSCs with both Li-TFSI and tBP. In (c), the area encircled by dashed line was originally capped by Au and small crystals in the uncapped area were labeled with yellow circles. (c3, c4) Top-view and cross-section SEM images of the uncapped area of the stressed PSCs with both Li-TFSI and tBP.

2.2. Relation between spiro-OMeTAD crystallization and PSC performance decline

In this section, we are showing the results of three experiments to reveal the relation between spiro-OMeTAD crystallization and deteriorated PSC performance.

In the first experiment, to exclude the possibility that the PSC degradation is caused by perovskite instability under thermal stress, we fabricated a stack consisting of ITO/SnO$_2$/PCBM/perovskite and stressed this stack at 85°C for 1000 hours. Afterwards, fresh spiro-OMeTAD and Au were deposited on this stressed stack. Their JV characteristics were compared with a freshly made PSC stack. As shown in Table S1, these two stacks show very similar PCE, Jsc, open-circuit voltage (Voc) and FF. This suggests the perovskite is stable at 85 °C and is not the main cause for PSC degradation.

In the second experiment, we investigated whether the PSC degradation is caused by the contact between Au and perovskite through the trenches. We fabricated a reference PSC with device structure ITO/SnO$_2$/PCBM/perovskite/Au. As shown in Figure S3, this reference PSC has a low Voc of 0.33 V. In contrast, the 85 °C stressed PSC has a much higher Voc of 0.96 V. It implies in this stressed PSC, Au was very likely not in contact with perovskite, just like the situation shown in Figure 1 (c2). We further removed the Au in the stressed PSC, and subsequently deposited fresh Au. As a result, PSC with fresh Au presents low Voc of 0.32 V, which is very similar to that of

the reference PSC. It suggests that part of fresh Au was directly deposited on perovskite through the trenches in the spiro-OMeTAD films. We can infer that if Au contacts perovskite through the trenches after the PSC is stressed at 85 °C, a huge reduction in Voc should be observed. However, after our 1032-hour stressing, Jsc and FF of stressed PSCs reduced drastically and Voc only declined slightly. Therefore, from this experiment we can conclude the PSC degradation at 85 °C is not caused by the contact between Au and perovskite.

In the third experiment, we removed Au and spiro-OMeTAD film in stressed PSCs and deposited fresh spiro-OMeTAD and Au. The process is illustrated in the schematics in Figure 2. As a result, the low Jsc, FF and thus the PCE of the stressed PSC almost recovered to their initial values. This result proves that it is the crystallized spiro-OMeTAD film that causes the PSC performance decline. Here, we further investigated the reason behind the drastically decreased Jsc and FF in the stressed PSC. The series resistance (Rs) of the PSC before stressing calculated from JV curves in Figure 2 was 6.45 Ωcm^2 and it increased to 66.30 Ωcm^2 upon stressing. According to the numerical simulation outcome shown in Figure S4, increasing Rs from 6.45 Ωcm^2 to 66.30 Ωcm^2 does drastically reduce Jsc and FF, while the Voc remained unchanged. This is in good agreement with the experimental results in Figure 2. We think two factors related to the spiro-OMeTAD film cause this increase in Rs. First, the contact area between perovskite and hole transport layer was reduced due to the emerged trenches. According to the resistance equation R=ρl/A, where ρ, l and A are the resistivity, length and cross-section area of the material, the resistance of spiro-OMeTAD film will increase due to its cross-section area reduction. Second, the phase transition of spiro-OMeTAD film from amorphous to crystalline could also change the resistivity of spiro-OMeTAD film as well as the contact resistance between spiro-OMeTAD film and its adjacent layers. These two factors together lead to the increased Rs.
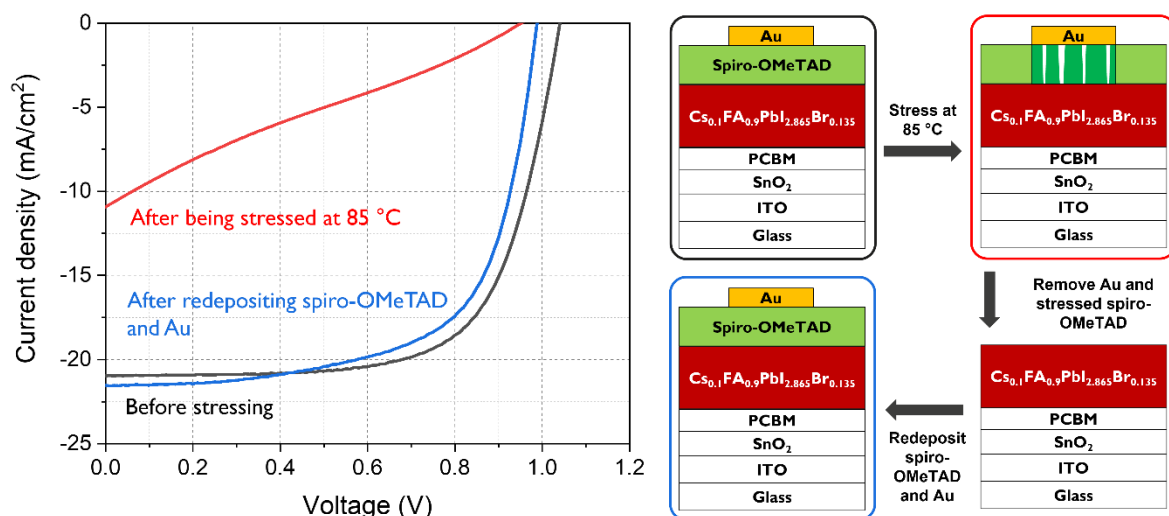
Figure 2. The stack schematics and their corresponding J-V curves of a PSC before stressing (black), after being stressed at 85 °C (red) and after redepositing spiro-OMeTAD and Au (blue).

Through these three experiments, we reach the conclusion that the drastic PCE decrease in 85 °C stressed PSCs is not caused by the damage of the perovskite layer. The unaffected perovskite quality and the fact that Au capping layer stays above the trenches instead of contacting perovskite together lead to little change in Voc. It is the creation of trenches by large domain spiro-OMeTAD crystallization that increases the Rs of PSC stack, reducing Jsc, FF and thus PCE. Yet, it is still not clear why the simultaneous presence of tBP and Au capping layer facilitates the large domain spiro-OMeTAD crystallization. In the following section, we will show our hypothesis about how tBP and Au capping layer influence spiro-OMeTAD crystallization in an 85 °C stressed PSC, and in this way the results in Figure 1 (c and c1-c4) will be explained.

2.3. Hypothesis of the mechanism of spiro-OMeTAD film morphology change in PSCs

As shown in the schematics in Figure 3 (a), in the beginning of 85 °C thermal stressing, due to the presence of large amount of tBP, the spiro-OMeTAD film is speculated to have a Tg lower than 85 °C. The speculation of spiro-OMeTAD Tg is discussed in Note S1 in the supporting

information. Therefore, such spiro-OMeTAD film with low Tg can easily crystallize at 85 °C. This explains the observed spiro-OMeTAD crystals at both Au capped area and uncapped area as shown in Figure 1 (c). As mentioned before, the large domain crystals of several millimeter range were only able to develop under the Au capping layer, while the crystals in the uncapped area were only up to about 10 µm. We conjecture that the following reasons lead to this phenomenon: at the uncapped area, the crystals grow not only laterally but also substantially rise above the amorphous surface[23,24], as sketched in Figure 3 (b). As evidenced by the SEM and AFM images in Figure S2 (a-d), the spiro-OMeTAD crystals rise several tens to 200 nm above the amorphous surface. Considering crystals are denser than its amorphous form[25], the lateral-upward spiro-OMeTAD crystallization will lead to a strong volume contraction in the lateral direction, quickly leaving gaps between the crystalline and amorphous areas, which can be clearly seen in Figure S2 (e and f). Once the gap is formed, it becomes impossible for molecules from the amorphous area to diffuse to and integrate into the crystal. In other words, the crystal growth stops. At the same time, the tBP at the uncapped area quickly evaporates, increasing the film Tg to above 85 °C (Figure 3 (b)). As a result, the chance for new crystal formation is reduced in the uncapped area. Eventually, most uncapped area remains amorphous.

At the Au-capped area, tBP also evaporate. However, the evaporation rate is slower than that in the uncapped area due to two possible reasons. Frist, the presence of the capping layer hinders the escape of tBP vapor. Second, pyridine is reported to adsorb on Au[26,26–28]. Thus, the presence of Au capping layer might further prevent the escape of tBP. As a result, the Tg of spiro-OMeTAD increases, but its increasing rate is slower than that of uncapped area (Figure 3 (b, c)). The remained low Tg (<85 °C) facilitates the spiro-OMeTAD crystallization. We exclude the possibility that the spiro-OMeTAD crystallization is caused by Au diffusion[29,30] or its Coulomb screening effect[31].

The reasoning can be found in Note S2, supporting information. Moreover, the tendency of spiro-OMeTAD crystals to rise above the amorphous surface is suppressed due to the presence of the Au capping layer. Consequently, the crystallized film remains flat as shown in Figure 1 (c2). In the lateral direction, the volume contraction is not as strong as that at the uncapped area so that a gap will not form between amorphous and crystalline areas. For this reason, the crystal can continuously grow as sketched in Figure 3 (b-d). In the end, when the crystal grows till the border between Au-capped and uncapped areas, the growth stops due to the higher film Tg at the uncapped area as shown in Figure 3 (d).
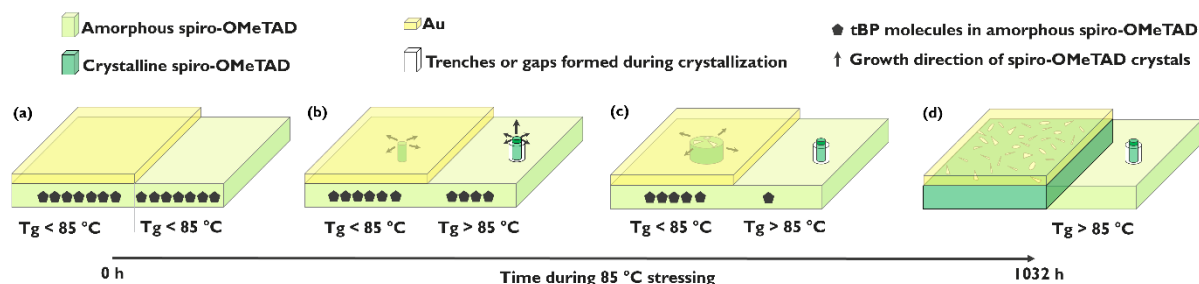

Figure 3. (a-d) Schematics showing the hypothesis of the mechanism of spiro-OMeTAD film morphology evolvement in PSCs during 1032-hour 85 °C thermal stressing.

2.4. Strategies to stabilize amorphous state of spiro-OMeTAD film.

According to our analysis and hypothesis, we hereby propose three strategies to hinder spiro-OMeTAD crystallization. The first strategy is to prevent the direct contact between Au and spiro-OMeTAD by inserting an extra layer. Hereby, MoO_x was applied, as it has been reported to work as an interlayer between spiro-OMeTAD and metal contact without affecting the PSC performance[32,33]. The second strategy is to reduce residual tBP via preheating bare spiro-OMeTAD film before subsequent layer deposition. Bailie et al. proved tBP evaporates at 85 °C from spiro-OMeTAD films[34]. And according to Malinauskas et al.[12], after being heated at 100 °C in argon environment for one week, the Tg of a 3 µm spiro-OMeTAD film with Li-TFSI and tBP increases

from 72 °C to 110 °C, and in another week the Tg reached 119 °C. Here in our work, as a proof-of-concept test, we chose to preheat the 250 nm spiro-OMeTAD film in stack at 85 °C for 13 days (312 hours) to reduce the tBP content in spiro-OMeTAD film, targeting to increase its Tg. This preheating condition certainly can be further optimized. In Note S3, corroborated by experimental data shown in Figure S6 and S7, we proposed routes to reduce the preheating duration to make the preheating process more practical. Finally, the third strategy is the combination of the previous two strategies. Thus, four types of PSCs were prepared and their performance under 85 °C stress was tracked through JV measurements. The first type is the reference PSCs with fresh spiro-OMeTAD and Au. In the second type of PSCs, a 10 nm MoO$_x$ layer was evaporated on fresh spiro-OMeTAD before Au deposition. In the third type of PSCs, spiro-OMeTAD films were preheated at 85 °C for 312 hours to reduce residual tBP prior to Au deposition. In the fourth type of PSCs, spiro-OMeTAD films were preheated at 85 °C for 312 hours and subsequently a 10 nm MoO$_x$ layer and Au were deposited.

As shown in Figure 4 (a), after being stressed at 85 °C for 1032 hours, the average PCE of the reference spiro-OMeTAD/Au PSCs significantly decreased from 15.4 % to 3.3%, with only 22% relative efficiency remaining. The POM image in Figure 4 (b) indicates the spiro-OMeTAD films crystallized. Top-view and cross-section SEM images in Figure 4 (b1 and b2) reveal empty trenches of several micrometers appeared at the area of capped spiro-OMeTAD. In contrast, the average PCE of spiro-OMeTAD/MoO$_x$/Au PSCs reduced from 15.5% - 15.7% to 8.9% - 9.2 %, retaining 57% - 60% relative PCE after the same stressing condition. The top-view POM image in Figure 4 (c) indicates the spiro-OMeTAD film remained amorphous. The top-view SEM image of the previously capped area in Figure 4 (c1) shows the spiro-OMeTAD film is closed. The cross-section SEM image of the capped area in Figure 4 (c2) reveals that there are voids with diameter

up to 80 nm present in the spiro-OMeTAD film. As suggested by Jena et al.[13], these voids can be the results of gaseous component produced and physically trapped in the space under the capping layer. Comparing spiro-OMeTAD/Au and spiro-OMeTAD/MoO$_x$/Au PSCs, it is clear that by changing the material in contact with spiro-OMeTAD from Au to MoO$_x$, the spiro-OMeTAD crystallization is prevented, leading to better PSC thermal stability. According to the discussion in section 2.3, the Au capping layer facilitates spiro-OMeTAD crystallization via preventing tBP evaporation due to its capping effect and its capability to adsorb tBP. Spiro-OMeTAD remains capped if an extra MoOx layer is applied. Thus, we speculate MoO$_x$ prevents tBP from adsorbing on the capping layer.
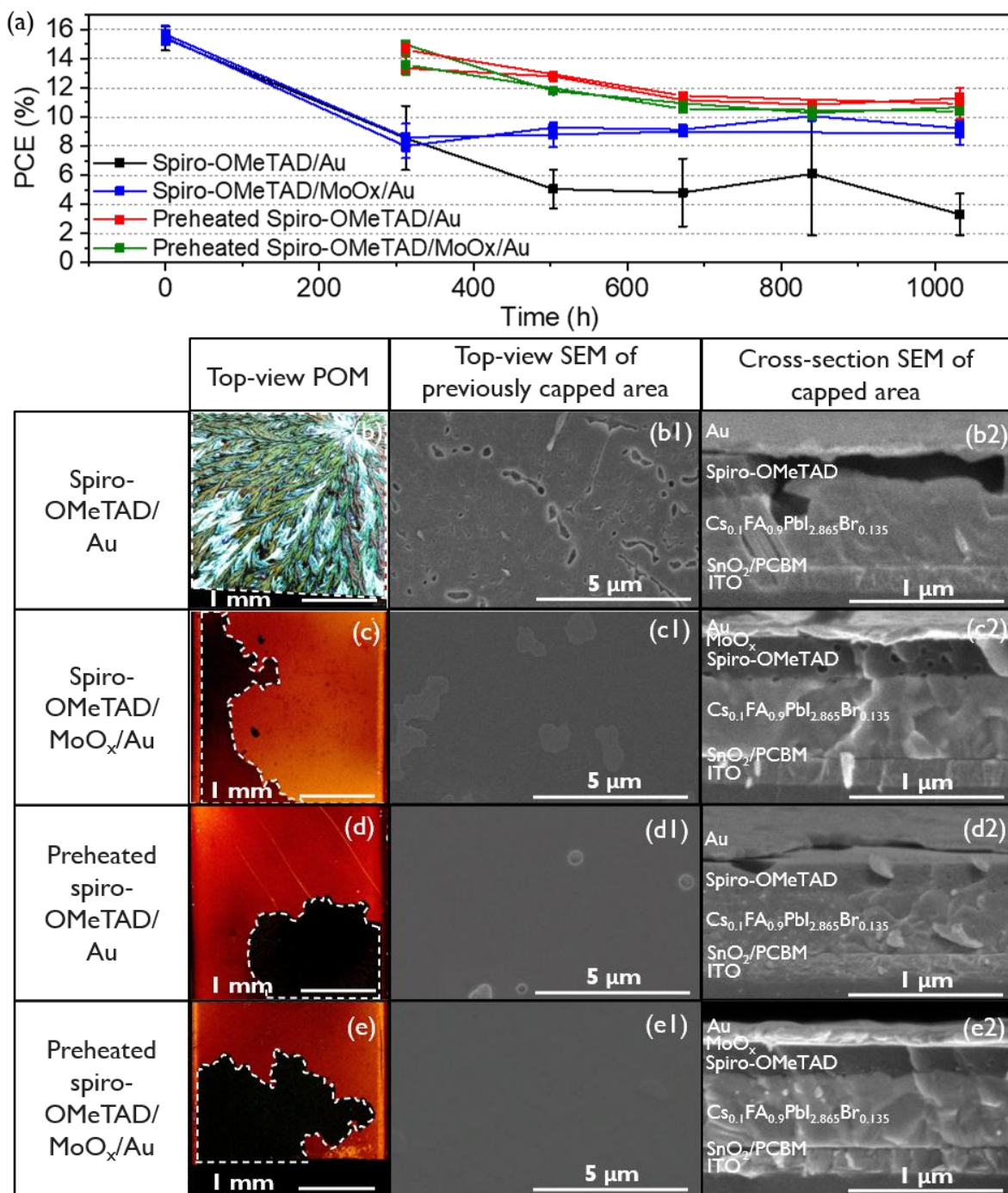
Figure 4. (a) PCE evolvement of four types of PSCs that were stressed at 85 °C in dark in nitrogen environment. Each data point represents mean value of 12 PSCs on one substrate and the error bars indicate the standard deviation. (b, b1, b2), (c, c1, c2), (d, d1, d2) and (e, e1, e2) are related to spiro-OMeTAD/Au, spiro-OMeTAD/MoO$_x$/Au, preheated Spiro-OMeTAD/Au and preheated

spiro-OMeTAD/MoO$_x$/Au PSCs, respectively. (b, c, d, e) Top-view POM images of the PSCs, where the dashed regions indicate the areas previously capped. (b1, c1, d1, e1) Top-view SEM images of the stressed spiro-OMeTAD film that were originally capped. (b2, c2, d2, e2) Cross-section SEM image of the stressed PSCs.

In the third type of PSCs, after preheating the stack ITO/SnO$_2$/PCBM/perovskite/spiro-OMeTAD at 85 °C for 312 hours, Au was evaporated on top of the preheated spiro-OMeTAD. As can be seen in Figure 4(a), the resultant preheated spiro-OMeTAD/Au PSCs show average PCE between 13.4% and 14.6%. After further thermal stress at 85 °C for 720 hours, the average PCE of preheated Spiro-OMeTAD/Au PSCs became 10.9% - 11.3%, retaining 75% - 85% relative PCE. The top-view POM image in Figure 4 (d) indicates the spiro-OMeTAD film remained amorphous after the total 1032-hour stressing. Both the top-view SEM image of the previously capped area and the cross-section SEM image of the capped area in Figure 4 (d1 and d2) reveal there are a few voids up to 0.7 µm in the spiro-OMeTAD film. Considering the results shown in Figure 1 (c-c4), we can deduce that during the first 312-hour thermal stressing, the bare spiro-OMeTAD film remains closed and smooth. The appearance of these voids should be caused by the Au capping layer deposited after the 312-hour stressing. As discussed before, these voids could be generated due to escape of tBP that adsorbed on Au. Despite these voids, these PSCs still retain relatively good performance compared to spiro-OMeTAD/Au and spiro-OMeTAD/MoO$_x$/Au PSCs. As shown in Figure 4 (a), in the fourth type of PSCs, after preheating ITO/SnO$_2$/PCBM/perovskite/spiro-OMeTAD stack at 85 °C for 312 hours, the completed preheated spiro-OMeTAD/MoO$_x$/Au PSCs show average PCE between 13.6% - 15.0%. With further stressing for 720 hours, the PCE became 10.4% - 10.7%, retaining 71% - 76% relative PCE. The top-view POM image in Figure 4 (d) indicates the spiro-OMeTAD film remained

amorphous after the total 1032-hour thermal stressing. The top-view SEM image of the previously capped area in Figure 4 (e1) reveals the spiro-OMeTAD film remained a close layer. The cross-section SEM image of the capped area in Figure 4 (e2) shows the spiro-OMeTAD film does not have significantly visible voids as those in the other three types of PSCs.

Comparing all four types of PSCs, we can conclude the three strategies are all effective in preventing spiro-OMeTAD crystallization, thus improving the PSC thermal stability. It is noticeable that PSCs containing preheated spiro-OMeTAD have lower initial PCEs, mainly due to lower FF (see Figure S5). Figure S8 shows the FF and Rs obtained from the initial JV curves of all four types of PSCs. It can be clearly seen the preheated devices have lower FF and higher Rs. The study from Kasparavicius et al.[35] proves the oxidized spiro-OMeTAD, i.e. spiro-OMeTAD[TFSI]$_x$ where x = 1 or 2, is fast reduced under thermal stress. Thus, in the preheated devices, as the reduction reaction carries on, the hole transporting capability and conductivity of spiro-OMeTAD film will accordingly decrease, leading to higher Rs thus lower FF and PCE. Despite of slightly lower initial PCE, the preheating strategy proves to be more effective than simply isolating spiro-OMeTAD from Au since the average PCE of preheated spiro-OMeTAD/Au PSCs and preheated spiro-OMeTAD/MoO$_x$/Au PSCs at 1032 hour are higher than that of spiro-OMeTAD/MoO$_x$/Au PSCs. This implies the PSC thermal stability could further improve through careful optimizing the preheating condition. From a morphology point of view, the combination of preheating spiro-OMeTAD and applying a MoO$_x$ interlayer is the most effective strategy to stabilize the morphology of spiro-OMeTAD. We infer for longer term thermal stressing, this combined strategy will lead to better stability compared to the other strategies.

It can be noticed there is still a relative 15%-30% PCE drop for the PSCs with best thermal stability. We deem the still existing 15%-30% PCE drop lies on the chemical instability of oxidized

spiro-OMeTAD. The study from Kasparavicius et al. [35] shows the oxidized spiro-OMeTAD, i.e. spiro-OMeTAD[TFSI]$_x$ where x = 1 or 2, is able to stay oxidized at room temperature for as long as 70 days. However, when subjecting to high temperature, which is 100 °C in their study, spiro-OMeTAD [TFSI]$_x$ is rapidly reduced. Spiro-OMeTAD [TFSI]$_x$ is the p-dopant in spiro-OMeTAD molecule matrix. In our experiment, during the 85 °C stressing of PSCs, the hole transporting capability and conductivity of spiro-OMeTAD film would decrease due to spiro-OMeTAD [TFSI]$_x$ reduction, thus lowering the PCE. According to Kasparavicius et al. [35], encapsulating the spiro-OMeTAD film is able to slow down the reduction reaction, however, not able to fully prevent it. Therefore, it appears the chemical state of spiro-OMeTAD [TFSI]$_x$ is intrinsically instable at high temperature. To solve this chemical instability issue, developing new oxidants for spiro-OMeTAD could be an effective route.

3. CONCLUSION

In conclusion, we have shown that the presence of tBP and Au capping layer are both the necessary elements that promote spiro-OMeTAD crystallization, increasing series resistance of PSCs and thus leading to PCE degradation. tBP plays the main role in promoting spiro-OMeTAD film crystallization by reducing its Tg, while Au capping layer prevents tBP evaporation due to its capping effect and possibly also its capability to adsorb tBP. According to our hypothesis, we demonstrated three strategies to stabilize the amorphous phase of spiro-OMeTAD film, i.e., preheating spiro-OMeTAD films, isolating spiro-OMeTAD from Au with MoO$_x$ layer and the combination of these two. Consequently, the thermal stability of the PSCs applying these three strategies is significantly improved. We infer the combined strategy with further optimized preheating condition will lead to even better PSCs thermal stability, providing a facile route to achieve highly efficient and thermally stable spiro-OMeTAD containing PSCs.

4. EXPERIMENTAL SECTION

4.1 Materials and experimental details

4.1.1 Materials

Table 1. Materials used in this work and their corresponding supplying companies.

Materials	Company
Tin oxide (SnO_2) nanoparticles, 15wt%	Alfa Aesar
PCBM	Nano-c
Lead Iodide (PbI_2)	TCI
Formamidinium iodide (FAI)	Greatcellsolar Materials
Formamidinium bromide (FABr)	Greatcellsolar Materials
Cesium iodide (CsI)	abcr
N, N-Dimethylformamide anhydrous, 99.8% (DMF)	Sigma-Aldrich
Dimethyl sulfoxide anhydrous, ≥ 99.9% (DMSO)	Sigma-Aldrich
tert-butylpyridine (tBP)	Sigma-Aldrich
Acetonitrile	Sigma-Aldrich
Lithium bis(trifluoromethanesulfonyl)imide (Li-TFSI)	Sigma-Aldrich
2,2',7,7'-tetrakis (N, N-di-p-methoxyphenyl-amine)9,9'-spirobifluorene (Spiro-OMeTAD)	Lumtec

4.1.2 Spiro-OMeTAD solution preparation

a) Spiro-OMeTAD solution: Dissolve 80 mg spiro-OMeTAD in 1 ml chlorobenzene.

b) Spiro-OMeTAD with Li-TFSI: Mix 1 ml of spiro-OMeTAD solution (80 mg/ml in chlorobenzene) with 17.5 µL Li-TFSI solution (520 mg/ml in acetonitrile).

c) Spiro-OMeTAD with both Li-TFSI and tBP, where the molar ratio between tBP and Li-TFSI is 7.2: Mix 1 ml of spiro-OMeTAD solution (80 mg/ml in chlorobenzene) with 17.5 µL Li-TFSI solution (520 mg/ml in acetonitrile) and 28.5 µL 4-tert-butylpyridine.

d) Spiro-OMeTAD with both Li-TFSI and tBP, where the molar ratio between tBP and Li-TFSI is 14.4: Mix 1 ml of spiro-OMeTAD solution (80 mg/ml in chlorobenzene) with 17.5 µL Li-TFSI solution (520 mg/ml in acetonitrile) and 57 µL 4-tert-butylpyridine.

4.1.3 Device fabrication

The ITO coated glass substrates were subsequently cleaned for 5 minutes in ultrasonic bath of detergent, deionized water, acetone, and isopropanol. The cleaned substrates were treated with UV-Ozone for 15 min. One part of 15 wt.% SnO_2 nanoparticle solution was diluted by 5 parts of deionized water. The resulting 2.5 wt.% solution was spin coated onto the glass/ITO substrate at 2800 rpm for 60 s. Then 10 mg/ml PCBM in chlorobenzene was spin coated at 2000 rpm for 30 s and annealed at 100 °C for 20 min. The perovskite solution was prepared and deposited using the method described in our previous work[36]. Then, the spiro-OMeTAD solution was dynamically spin-coated onto the perovskite films at 2000 rpm for 60 s. The perovskite films coated with Spiro-OMeTAD were exposed to air with 20% RH overnight to facilitate oxidization of spiro-OMeTAD. In devices with MoO_x, 10 nm MoO_x was thermally evaporated in vacuum. Eventually the devices were completed by thermal evaporation of 80 nm thick Au in vacuum through shadow masks. While measuring the cells, illumination masks are applied, defining active area of 0.08 cm^2.

4.1.4 Removal of Au (and MoOx) layer and spiro-OMeTAD layer

The Au (and MoO$_x$) layer was removed using scotch tapes. When Au was not visible on top of spiro-OMeTAD anymore, the spiro-OMeTAD layer was removed by spin coating 300 µl chlorobenzene on it at 2000 rpm for 60 s.

4.2 Characterization

4.2.1 Thermal stability measurement

PSCs were placed on a hotplate at 85 °C in a nitrogen filled glovebox in dark environment. JV measurements were performed in a nitrogen filled glovebox after the PSCs were cooled to room temperature using a Keithley 2602A source-measure unit and an Abet solar simulator with simulated AM1.5G illumination (Abet Sun 2000). The light irradiance was calibrated by a KG5 band pass equipped with ISE Fraunhofer certified Si photodiode. The devices were measured from -0.2 V to 1.2 V with a scan speed of 1 V/s. 3 rounds of JV measurement were performed with interval of 1 min. The second-round measurement was used for plotting and analysis.

4.2.2 Polarized optical microscopic imaging

Polarized optical microscopic images were obtained from Olympus AX70 microscope.

4.2.3 Scanning electron microscopic imaging

Scanning electron microscopic images were obtained from FEI Nova 200 scanning electron microscope.

4.2.4 Atomic force microscopic imaging

Atomic force microscopic imaging performed using Bruker Multimode 8 AFM (Santa Clara, CA, USA) with a Nanoscope V controller. Peak-Force Quantum Nano-Mechanics (PF-QNM) analytic technique was used to obtain topographical and qualitative mechanical data of spiro-OMeTAD layer. Probe used is TAP150A, Bruker.

4.3 Analysis and simulation method

4.3.1. Calculation of series resistance

$$Rs = \left. \frac{\partial V}{\partial J} \right|_{V = V_{oc}} \tag{1}$$

4.3.2 Numerical simulation

The numerical simulation is performed with software SCAPS developed at ELIS, University of Gent[36].

ASSOCIATED CONTENT

Supporting Information

Additional experimental results including PSC JV characteristics; SEM and AFM images; numerical simulation results. Additional notes on speculation of spiro-OMeTAD film Tg; discussion about the role of Au capping layer on spiro-OMeTAD film crystallization; potential routes to reduce preheating duration.

AUTHOR INFORMATION

Corresponding Author

*Wenya Song wenya.song@imec.be; *Jef Poortmans jef.poortmans@imec.be

Author Contribution

W.S. was the main contributor to the experimental part of this work and fabricated and characterized the solar cells, analyzed the data, and prepared the first draft of the manuscript and figures. W.S. and L.R. designed the experiments. R.T.E. conducted AFM and analyzed the data. W.Q. supported the solar cell fabrication and device analysis. W.Q., J.P.B., R.G., Y.K., A.H., T.A. and J.P. contributed to the scientific content through scientific discussions. J.P. was the main responsible PI and supervised the experimental work and the writing. All authors have read and given input to the final draft of this manuscript.

Notes

The authors declare no competing financial interest.

REFERENCES

(1)   NREL. Best Research-Cell Efficiencies https://www.nrel.gov/pv/assets/pdfs/best-research-cell-efficiencies-rev210726.pdf.

(2)   Shi, L.; Bucknall, M. P.; Young, T. L.; Zhang, M.; Hu, L.; Bing, J.; Lee, D. S.; Kim, J.; Wu, T.; Takamure, N.; McKenzie, D. R.; Huang, S.; Green, M. A.; Ho-Baillie, A. W. Y. Gas Chromatography-Mass Spectrometry Analyses of Encapsulated Stable Perovskite Solar Cells. *Science* **2020**, *368* (6497), eaba2412. https://doi.org/10.1126/science.aba2412.

(3)   Cheacharoen, R.; Boyd, C. C.; Burkhard, G. F.; Leijtens, T.; Raiford, J. A.; Bush, K. A.; Bent, S. F.; McGehee, M. D. Encapsulating Perovskite Solar Cells to Withstand Damp Heat and Thermal Cycling. *Sustain. Energy Fuels* **2018**, *2* (11), 2398–2406. https://doi.org/10.1039/c8se00250a.

(4)   Boyd, C. C.; Cheacharoen, R.; Bush, K. A.; Prasanna, R.; Leijtens, T.; Mcgehee, M. D. Barrier Design to Prevent Metal-Induced Degradation and Improve Thermal Stability in Perovskite Solar Cells. *ACS Energy Lett* **2018**, *3*, 1772–1778. https://doi.org/10.1021/acsenergylett.8b00926.

(5)   Gehlhaar, R.; Merckx, T.; Qiu, W.; Aernouts, T. Outdoor Measurement and Modeling of Perovskite Module Temperatures. *Glob. Challenges* **2018**, *2* (7), 1800008. https://doi.org/10.1002/gch2.201800008.

(6)   Gok, A.; Ozkalay, E.; Friesen, G.; Frontini, F. The Influence of Operating Temperature on the Performance of BIPV Modules. *IEEE J. Photovoltaics* **2020**, *10* (5), 1371–1378. https://doi.org/10.1109/JPHOTOV.2020.3001181.

(7)   Jiang, Q.; Zhao, Y.; Zhang, X.; Yang, X.; Chen, Y.; Chu, Z.; Ye, Q.; Li, X.; Yin, Z.; You, J. Surface Passivation of Perovskite Film for Efficient Solar Cells. *Nat. Photonics* **2019**, *13* (7), 460–466. https://doi.org/10.1038/s41566-019-0398-2.

(8)   Kim, M.; Kim, G. H.; Lee, T. K.; Choi, I. W.; Choi, H. W.; Jo, Y.; Yoon, Y. J.; Kim, J. W.; Lee, J.; Huh, D.; Lee, H.; Kwak, S. K.; Kim, J. Y.; Kim, D. S. Methylammonium Chloride Induces Intermediate Phase Stabilization for Efficient Perovskite Solar Cells. *Joule* **2019**, *3* (9), 2179–2192. https://doi.org/10.1016/j.joule.2019.06.014.

(9)   Zhu, H.; Liu, Y.; Eickemeyer, F. T.; Pan, L.; Ren, D.; Ruiz-Preciado, M. A.; Carlsen, B.; Yang, B.; Dong, X.; Wang, Z.; Liu, H.; Wang, S.; Zakeeruddin, S. M.; Hagfeldt, A.; Dar, M. I.; Li, X.; Grätzel, M. Tailored Amphiphilic Molecular Mitigators for Stable Perovskite Solar Cells with 23.5% Efficiency. *Adv. Mater.* **2020**, *32* (12), 1907757. https://doi.org/10.1002/adma.201907757.

(10)   Lu, H.; Liu, Y.; Ahlawat, P.; Mishra, A.; Tress, W. R.; Eickemeyer, F. T.; Yang, Y.; Fu, F.; Wang, Z.; Avalos, C. E.; Carlsen, B. I.; Agarwalla, A.; Zhang, X.; Li, X.; Zhan, Y.; Zakeeruddin, S. M.; Emsley, L.; Rothlisberger, U.; Zheng, L.; Hagfeldt, A.; Grätzel, M. Vapor-Assisted Deposition of Highly Efficient, Stable Black-Phase FAPbI3 Perovskite Solar Cells. *Science* **2020**, *370* (6512). https://doi.org/10.1126/science.abb8985.

(11)   Jena, A. K.; Numata, Y.; Ikegami, M.; Miyasaka, T. Role of Spiro-OMeTAD in Performance Deterioration of Perovskite Solar Cells at High Temperature and Reuse of the Perovskite Films to Avoid Pb-Waste. *J. Mater. Chem. A* **2018**, *6*, 2219–2230. https://doi.org/10.1039/C7TA07674F.

(12)   Malinauskas, T.; Tomkute-Luksiene, D.; Sens, R.; Daskeviciene, M.; Send, R.; Wonneberger, H.; Jankauskas, V.; Bruder, I.; Getautis, V. Enhancing Thermal Stability and Lifetime of Solid-State Dye-Sensitized Solar Cells via Molecular Engineering of the Hole-Transporting Material Spiro-OMeTAD. *ACS Appl. Mater. Interfaces* **2015**, *7* (21), 11107–11116. https://doi.org/10.1021/am5090385.

(13)   Jena, A. K.; Ikegami, M.; Miyasaka, T. Severe Morphological Deformation of Spiro-OMeTAD in $(CH_3NH_3)PbI_3$ Solar Cells at High Temperature. *ACS Energy Lett.* **2017**, *2* (8), 1760–1761. https://doi.org/10.1021/acsenergylett.7b00582.

(14)   Schloemer, T. H.; Christians, J. A.; Luther, J. M.; Sellinger, A. Doping Strategies for Small Molecule Organic Hole-Transport Materials: Impacts on Perovskite Solar Cell Performance and Stability. *Chem. Sci.* **2019**, *10* (7), 1904–1935. https://doi.org/10.1039/C8SC05284K.

(15)   Snaith, H. J.; Grätzel, M. Enhanced Charge Mobility in a Molecular Hole Transporter via Addition of Redox Inactive Ionic Dopant: Implication to Dye-Sensitized Solar Cells. *Appl. Phys. Lett.* **2006**, *89* (26), 262114. https://doi.org/10.1063/1.2424552.

(16)   Abate, A.; Leijtens, T.; Pathak, S.; Teuscher, J.; Avolio, R.; Errico, M. E.; Kirkpatrik, J.; Ball, J. M.; Docampo, P.; McPherson, I.; Snaith, H. J. Lithium Salts as "Redox Active" p-Type Dopants for Organic Semiconductors and Their Impact in Solid-State Dye-Sensitized Solar Cells. *Phys. Chem. Chem. Phys.* **2013**, *15* (7), 2572. https://doi.org/10.1039/c2cp44397j.

(17)   Wang, S.; Huang, Z.; Wang, X.; Li, Y.; Günther, M.; Valenzuela, S.; Parikh, P.; Cabreros, A.; Xiong, W.; Meng, Y. S. Unveiling the Role of TBP-LiTFSI Complexes in Perovskite

Solar Cells. *J. Am. Chem. Soc.* **2018**, *140* (48), 16720–16730. https://doi.org/10.1021/jacs.8b09809.

(18) Zhang, J.; Zhang, T.; Jiang, L.; Bach, U.; Cheng, Y. B. 4- Tert-Butylpyridine Free Hole Transport Materials for Efficient Perovskite Solar Cells: A New Strategy to Enhance the Environmental and Thermal Stability. *ACS Energy Lett.* **2018**, *3* (7), 1677–1682. https://doi.org/10.1021/acsenergylett.8b00786.

(19) Ren, Y.; Ren, M.; Xie, X.; Wang, J.; Cai, Y.; Yuan, Y.; Zhang, J.; Wang, P. A Spiro-OMeTAD Based Semiconductor Composite with over 100 °C Glass Transition Temperature for Durable Perovskite Solar Cells. *Nano Energy* **2021**, *81*, 105655. https://doi.org/10.1016/j.nanoen.2020.105655.

(20) Barranco, A.; Lopez-Santos, M. C.; Idigoras, J.; Aparicio, F. J.; Obrero-Perez, J.; Lopez-Flores, V.; Contreras-Bernal, L.; Rico, V.; Ferrer, J.; Espinos, J. P.; Borras, A.; Anta, J. A.; Sanchez-Valencia, J. R. Enhanced Stability of Perovskite Solar Cells Incorporating Dopant-Free Crystalline Spiro-OMeTAD Layers by Vacuum Sublimation. *Adv. Energy Mater.* **2020**, *10* (2), 1901524. https://doi.org/10.1002/aenm.201901524.

(21) Khenkin, M. V.; Anoop, K. M.; Visoly-Fisher, I.; Galagan, Y.; Di Giacomo, F.; Patil, B. R.; Sherafatipour, G.; Turkovic, V.; Rubahn, H. G.; Madsen, M.; Merckx, T.; Uytterhoeven, G.; Bastos, J. P. A.; Aernouts, T.; Brunetti, F.; Lira-Cantu, M.; Katz, E. A. Reconsidering Figures of Merit for Performance and Stability of Perovskite Photovoltaics. *Energy Environ. Sci.* **2018**, *11* (4), 739–743. https://doi.org/10.1039/c7ee02956j.

(22) Juarez-Perez, E. J.; Leyden, M. R.; Wang, S.; Ono, L. K.; Hawash, Z.; Qi, Y. Role of the

Dopants on the Morphological and Transport Properties of Spiro-MeOTAD Hole Transport Layer. *Chem. Mater.* **2016**, *28* (16), 5702–5709. https://doi.org/10.1021/acs.chemmater.6b01777.

(23)   Suna, Y.; Zhua, L.; Kearnsa, K. L.; Edigera, M. D.; Yua, L. Glasses Crystallize Rapidly at Free Surfaces by Growing Crystals Upward. *Proc. Natl. Acad. Sci. U. S. A.* **2011**, *108* (15), 5990–5995. https://doi.org/10.1073/pnas.1017995108.

(24)   Sun, Y.; Zhu, L.; Wu, T.; Cai, T.; Gunn, E. M.; Yu, L. Stability of Amorphous Pharmaceutical Solids: Crystal Growth Mechanisms and Effect of Polymer Additives. *AAPS J.* **2012**, *14* (3), 380–388. https://doi.org/10.1208/s12248-012-9345-6.

(25)   Myerson, A. S.; Erdemir, D.; Lee, A. Y. Crystals and Crystal Growth. In *Handbook of Industrial Crystallization*; Cambridge University Press, 2019; pp 32–75. https://doi.org/10.1017/9781139026949.002.

(26)   Stolberg, L.; Lipkowski, J.; Irish, D. E. Adsorption of Pyridine at the Au(311)-Solution Interface. *J. Electroanal. Chem.* **1992**, *322*, 357–372. https://doi.org/10.1016/0022-0728(92)80088-L.

(27)   Stolberg, L.; Richer, J.; Lipkowski, J.; Irish, D. E. Adsorption of Pyridine at the Polycrystalline Gold-Solution Interface. *J. Electroanal. Chem.* **1986**, *207*, 213–234. https://doi.org/10.1016/0022-0728(86)87073-5.

(28)   Stolberg, L.; Lipkowski, J.; Irish, D. E. Adsorption of Pyridine at the Au(311)-Solution Interface. *J. Electroanal. Chem.* **1987**, *238*, 333–353. https://doi.org/10.1016/0022-0728(92)80088-L.

(29)   Cacovich, S.; Ciná, L.; Matteocci, F.; Divitini, G.; Midgley, P. A.; Di Carlo, A.; Ducati, C.
Gold and Iodine Diffusion in Large Area Perovskite Solar Cells under Illumination.
Nanoscale **2017**, *9* (14), 4700–4706. https://doi.org/10.1039/C7NR00784A.

(30)   Domanski, K.; Correa-Baena, J. P.; Mine, N.; Nazeeruddin, M. K.; Abate, A.; Saliba, M.;
Tress, W.; Hagfeldt, A.; Grätzel, M. Not All That Glitters Is Gold: Metal-Migration-Induced
Degradation in Perovskite Solar Cells. *ACS Nano* **2016**, *10* (6), 6306–6314.
https://doi.org/10.1021/acsnano.6b02613.

(31)   *Metal-Induced Crystallization: Fundamentals and Applications*, 1st ed.; Wang, Z.,
Jeurgens, L. P. H., Mittemeijer, E. J., Eds.; Taylor & Francis Group, LLC, 2015.

(32)   Christians, J. A.; Schulz, P.; Tinkham, J. S.; Schloemer, T. H.; Harvey, S. P.; Tremolet De
Villers, B. J.; Sellinger, A.; Berry, J. J.; Luther, J. M. Tailored Interfaces of Unencapsulated
Perovskite Solar Cells for >1,000 Hour Operational Stability. *Nat. Energy* **2018**, *3* (1), 68–
74. https://doi.org/10.1038/s41560-017-0067-y.

(33)   Sanehira, E. M.; Tremolet de Villers, B. J.; Schulz, P.; Reese, M. O.; Ferrere, S.; Zhu, K.;
Lin, L. Y.; Berry, J. J.; Luther, J. M. Influence of Electrode Interfaces on the Stability of
Perovskite Solar Cells: Reduced Degradation Using MoOx/Al for Hole Collection. *ACS
Energy Lett.* **2016**, *1* (1), 38–45. https://doi.org/10.1021/acsenergylett.6b00013.

(34)   Bailie, C. D.; Unger, E. L.; Zakeeruddin, S. M.; Grätzel, M.; McGehee, M. D. Melt-
Infiltration of Spiro-OMeTAD and Thermal Instability of Solid-State Dye-Sensitized Solar
Cells. *Phys. Chem. Chem. Phys.* **2014**, *16* (10), 4864–4870.
https://doi.org/10.1039/c4cp00116h.

(35) Kasparavicius, E.; Magomedov, A.; Malinauskas, T.; Getautis, V. Long-Term Stability of the Oxidized Hole-Transporting Materials Used in Perovskite Solar Cells. *Chem. - A Eur. J.* **2018**, *24* (39), 9910–9918. https://doi.org/10.1002/CHEM.201801441.

(36) Burgelman, M.; Nollet, P.; Degrave, S. Modelling Polycrystalline Semiconductor Solar Cells. *Thin Solid Films* **2000**, *361*, 527–532. https://doi.org/10.1016/S0040-6090(99)00825-1.